Int J Fract (2025) 249:19
https://doi.org/10.1007/s10704-024-00821-3

RESEARCH

Phase field modeling of anisotropic silicon crystalline cracking in 3D thin-walled photovoltaic laminates

Z. Liu · P. Lenarda · J. Reinoso · M. Paggi

Received: 26 May 2024 / Accepted: 15 November 2024 / Published online: 31 January 2025

Abstract A novel computational framework integrating the phase field approach with the solid shell formulation at finite deformation is proposed to model the anisotropic fracture of silicon solar cells in the thin-walled photovoltaic laminates. To alleviate the locking effects, both the enhanced assumed strain and assumed natural strain methods are incorporated in the solid shell element formulation. Aiming at tackling the poor convergence performance of standard Newton schemes, the efficient and robust quasi-Newton scheme is adopted for the solution of phase field modeling with enhanced shell formulation in a monolithic manner. Due to fracture anisotropy of the brittle silicon solar cells, the second-order structural tensor that is defined by the normal of preferential crack plane is introduced into the crack energy density function in the phase field modeling. On the other hand, to efficiently predict the crack growth of silicon solar cells, a global–local approach in the 3D setting proposed in the previous work is adopted here for the fracture modeling. In this approach, both mechanical deformation and phase field fracture are accounted for at the local model, while only mechanical deformation is addressed at the global level. At each time step, the solution of the global model is used to drive the local model, which corresponds to the one-way coupling in line with experimental evidence that the silicon cell cracking has negligible influence on the stiffness of photovoltaic modules. The capability of the modeling framework is demonstrated through numerical simulation of silicon solar cell cracking in the photovoltaic modules when subjected to different loading cases.

Keywords Global–local approach · Phase field fracture · Solid shell element · Quasi–Newton scheme

Z. Liu · P. Lenarda · M. Paggi
IMT School for Advanced Studies, Piazza San Francesco 19, 55100 Lucca, Italy
e-mail: zeng.liu@alumni.imtlucca.it

Z. Liu· J. Reinoso (✉)
Grupo de Ingeniería de Estructuras y Materiales. Departamento de Mecánica de Medios Continuos y Teoría de Estructuras, ETS Ingeniería, Universidad de Sevilla, Camino de los Descubrimientos S/N, 41092 Seville, Spain
e-mail: jreinoso@us.es

J. Reinoso
Escuela Politécnica Superior, Universidad de Sevilla, C/ Virgen de África, 7, Sevilla 41011, Spain

J. Reinoso
ENGREEN - Laboratory of Engineering for Energy and Environmental Sustainability, Universidad de Sevilla, Seville, Spain

1 Introduction

Nowadays, crystalline silicon photovoltaic (PV) modules have been massively deployed all over the world since the last century, and according to Xu et al. (2021), the installed capacity of PV approximately increases from 40 GW to 715 GW in the recent 10 years. Among the major components of PV products, including tempered glass, ethylene-co-vinyl acetate (EVA), silicon cells, and backsheet, the silicon wafer accounts for

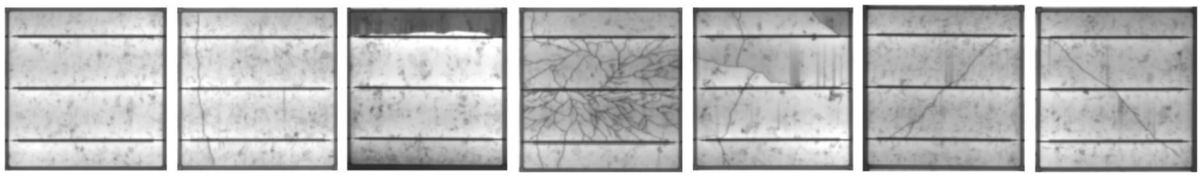

Fig. 1 Different crack patterns in silicon solar cells (Papargyri et al. 2020)

more than 40% of the manufacturing cost of crystalline modules (Papargyri et al. 2020). It was proposed in the 2010 International Technology Roadmap for Photovoltaics that the thickness of silicon cell should be significantly decreased so as to save cost of cystalline PV modules. However, the decrease of silicon cell thickness could reduce its robustness under mechanical loading and potentially leading to the formation of microcracking events within the conductor layer. Hence, the identification of crack initiation and propagation that may trigger performance degradation of PV modules has received a lot of attention in the recent decades.

During the fabrication process of silicon solar cells, permanent deformations are induced from the thermomechanical loadings, which corresponds to the residual stress that leads to cracks. It was pointed out in Rupnowski and Sopori (2009) that 2% of the silicon wafers present defects, causing the increase of production cost and material losses. Even though the fabrication process can be optimized, the imperfections inside the silicon cells during production are unavoidable, especially when the wafer thickness is reduced (Pingel et al. 2009; Liu et al. 2023). Besides, crack formation of silicon cells can also take place during the transportation and installation of PV modules in the field, as well as during the operation when subjected to the harsh environmental conditions such as wind, snow loading, hail impacts and so on Köntges et al. (2016), Assmus et al. (2011), Liu et al. (2023), Liu et al. (2022). The cracks of silicon solar cells are usually invisible, but could produce over time due to ageing electrically disconnected regions that significantly increase the electrical resistance, and hence reduce the power output of PV modules. Overall, the length, width and orientation of cracks in the silicon wafers directly influence the output of solar panels as pointed out in Munoz et al. (2011), Javvaji et al. (2018), Buerhop et al. (2018). According to the survey of over 200 PV modules, more than 20% of power loss has been detected due to the cell cracks in combination with EVA delamination and degradation (Käsewieter et al. 2014). Experimental studies in Chaturvedi et al. (2013) reported that approximately 4% power degradation are caused by cracks of solar cells in the mechanical load tests. When the disconnected cell area caused by crack formation and propagation is greater than 8% of the total cell layer, the associated power loss was found to be roughly proportional to the electrically inactive area (Köntges et al. 2017). Regarding the crack direction in solar cells, several types of cracks can be observed from previous experimental studies, including parallel and perpendicular cracks, $+45$ and -45 cracks, and multiple direction cracks (Kajari-Schröder et al. 2011), as shown in Fig. 1. Different cracks lead to different power degradation of PV modules. Therefore, it is of utmost importance to develop reliable simulation tools for the fracture modeling of brittle solar cells in order to understand the impact of cracks on the performance of PV modules.

In order to accurately predict the failure and crack propagation, several formulations on the basis of different numerical techniques have been developed in the past decades. Simplified phenomenological cohesive zone models specific for the crack modeling along internal boundaries have been proposed in Paggi and Wriggers (2011a), Paggi and Wriggers (2011b), Paggi et al. (2013), Paggi and Wriggers (2012), Infuso et al. (2014), in which cracking events are triggered by the evaluation of traction-separation constitutive laws. This modeling technique has been widely employed to identify crack paths along the element edges by incorporating a characteristic length scale, see the discussions in Ortiz and Pandolfi (1999), Paggi et al. (2013), Mergheim et al. (2005), Mergheim and Steinmann (2006), Spannraft et al. (2023), among many others. In contrast to the cohesive zone models, the extended finite element method has also been developed to model crack propagation, and it does not explicitly depend on the finite element discretization corresponding to the physical domain (Moës et al. 1999). Other alternative computational techniques such as enhanced finite ele-

ment method (Simo et al. 1993; Oliver et al. 2006) and generalized finite element method (Simone et al. 2006), can also be used to model crack events although possible operative difficulties to identify crack initiation and paths might arise. In order to overcome the disadvantages of the above-mentioned explicit modeling method for complex crack topologies, the phase field approach (Miehe et al. 2010a; Borden et al. 2012) that is based on the Griffith's theory has been proposed to address the crack modeling of quasi-brittle materials such as silicon solar cells (Paggi et al. 2018; Carollo et al. 2017). In this approach, the sharp crack is generally diffused through the definition of so-called phase field variable and the crack propagation is characterized by the evolution of the corresponding governing equations. According to the Γ-convergence theory in Francfort and Marigo (1998), the crack discontinuities are regularized by a characteristic phase field length scale. Note that the phase field formulation shares several common aspects with the gradient enhanced damage formulations, which is one of the most appealing advantages of this crack modeling method (Frémond and Nedjar 1996; Peerlings et al. 2001; Comi and Perego 2001). In view of this feature, the phase field approach accounting for thermodynamic consistency (Miehe et al. 2010a; Hofacker and Miehe 2013) has been extended to the modeling of ductile fracture (Ambati et al. 2015), anisotropic fracture (Gültekin et al. 2016), multiphysics fracture (Miehe et al. 2015), and polycrystalline materials (Clayton and Knap 2015, 2016), among many others. Given the promising aspects of phase field approach, this technique has been employed to model the crack propagation of brittle silicon solar cells in this work.

As mentioned above, to reduce the production cost of silicon solar panels, the average thickness of solar cells has decreased from 300 μm to 150 μm during the recent decades (Wohlgemuth et al. 2008; Terheiden et al. 2015; Wang 2006), which increases the breakage rates and crack events. Based on the computational framework developed in Liu et al. (2022), the solid shell formulation combined with anisotropic phase field model at finite deformation is proposed to model the preferential crack propagation in thin-film solar cells. In the literature, phase field models have been coupled with shell kinematics for the fracture modeling of thin-walled structures through many different ways, see Liu et al. (2022), Reinoso et al. (2017) and references therein. Previous attempts in Ulmer et al. (2012) have been made to model geometrically linear problems according to the Reissner-Midlin theory, but the developments are limited to standard finite elements. Alternative investigation adopting the Local Maximum-Entropy approximation is proposed in Amiri et al. (2014), making it difficult to be implemented into the standard finite element method. The tension-compression split method by integrating the energy contribution through the shell element thickness has been proposed in Paul et al. (2020), Kiendl et al. (2016), and later extended to the isogeometric modeling of multipatch structures (Proserpio et al. 2020; Paul et al. 2020). Recently, this approach has been adopted in Kikis et al. (2021), Pillai et al. (2020) for phase field fracture modeling of the Reissner-Mindlin shells and plates. Besides, other models have been developed in combination of phase field theory with solid shell and Kirchhoff-Love formulations to model brittle and ductile fracture (Reinoso et al. 2017; Ambati and De Lorenzis 2016; Areias et al. 2016; Proserpio et al. 2021). Hence, the attempt to employ the phase field solid shell formulation, extended to account for the anisotropic fracture orientation, is a proper choice for the crack modeling of solar cells in thin-walled PV laminates.

The structure of this work is organized as follows. In Sect. 2, the primary aspects of phase field approach for fracture modeling and solid shell kinematics at finite deformation are described in detail. The numerical implementation and quasi-Newton monolithic solution scheme are outlined in Sect. 3. Then the numerical examples are presented in Sect. 4, and finally some concluding remarks are summarized in Sect. 5.

2 Phase field solid shell formulation

In this section, the phase field solid shell formulation is presented for the modeling of anisotropic crack propagataion in the thin-film brittle solar cells. Firstly, the basics of phase field approach are revisited in Sect. 2.1. For a more comprehensive description, the detailed derivation of this theory can be found in the significant work (Miehe et al. 2010a; Miehe et al. 2010b; Bourdin et al. 2000). In Sect. 2.2, the solid shell kinetics at finite deformation are described in the convective curvilinear coordinate system.

2.1 Basics of the phase field approach to fracture

In the 3D setting, let $\mathcal{B}_0 \subset \mathbb{R}^3$ and $\mathcal{B}_t \subset \mathbb{R}^3$ denote the reference configuration and current configuration of an arbitrary solid body with existing crack represented by Γ, and $\mathbf{X}$ and $\mathbf{x}$ stand for the position vectors in the corresponding configurations, respectively. Furthermore, let $\partial\mathcal{B}_0$ and $\partial\mathcal{B}_t$ be the exterior boundary of the solid body in the reference and current configuration, respectively. The motion of the material point $\mathbf{X}$ inside the body is denoted by $\boldsymbol{\varphi}(\mathbf{X}, t) : \mathcal{B}_0 \times [0, t] \rightarrow \mathbb{R}^3$ that maps into the corresponding position $\mathbf{x}$ in the current configuration during the time interval $[0, t]$. The deformation gradient $\mathbf{F}^u$ is defined as $\mathbf{F}^u := \partial_{\mathbf{X}}\boldsymbol{\varphi}(\mathbf{X}, t)$, where $\partial_{\mathbf{X}}$ represents the partial derivative with respect to the position $\mathbf{X}$ in the reference configuration, and its determinant $J^u = \det[\mathbf{F}^u]$ denotes the Jacobian. The phase field approach is conceived as the regularization of sharp crack topology within a diffusive crack zone characterized by the scalar-valued function $\mathfrak{d} : \mathcal{B}_0 \times [0, t] \rightarrow [0, 1]$ to model brittle fracture. The phase field variable $\mathfrak{d}$ smears out the sharp crack by a diffusive crack area of width l, as shown in Fig. 2. It is noted that the width of regularization area depends on the parameter l, which is called the phase field length scale that controls the transition between intact and damaged parts. In the modeling framework, $\mathfrak{d}$ is regarded as a smooth function of $(\mathbf{X}, t)$, and $\mathfrak{d} = 0$ and $\mathfrak{d} = 1$ denote intact and cracked states, respectively.

According to the variational theory of fracture (Bourdin et al. 2000), the total energy functional that governs the cracked body under external loadings takes the form of

$$\Pi(\mathbf{u}, \Gamma) = \Pi_{\text{int}}(\mathbf{u}, \mathfrak{d}, \Gamma) + \Pi_{\text{ext}}(\mathbf{u}) \tag{1}$$

where $\mathbf{u}$ denotes the displacement field, and Π_{int} and Π_{ext} represent the internal and external energy functionals, respectively. Note that the internal energy functional term Π_{int} is defined as the sum of elastic energy stored in the solid body $\Pi_{\mathcal{B}}$ and the energy dissipated through crack propagation Π_{Γ}. Based on the Griffith's theory, the internal energy functional Π_{int} is defined as

$$\begin{aligned}\Pi_{\text{int}}(\mathbf{u}, \mathfrak{d}, \Gamma) &= \Pi_{\mathcal{B}}(\mathbf{u}, \mathfrak{d}) + \Pi_{\Gamma}(\Gamma) \\ &= \int_{\mathcal{B}\setminus\Gamma} \Psi(\mathbf{u}, \mathfrak{d})\, \mathrm{d}\Omega + \int_{\Gamma} \mathcal{G}_c\, \mathrm{d}\Gamma\end{aligned} \tag{2}$$

where Ψ denotes the specific elastic energy, and $\mathcal{G}_c$ is the critical energy release rate. The dissipated fracture energy during the crack propagation is evaluated through the Griffith theory. It should be pointed out that the competition between the elastic energy in the solid body and fracture energy is directly defined in the context of minimization problem. The evaluation of this competition is computationally challenging when the space discretization methods are used to track the crack propagation. To circumvent the use of tracking algorithms, the phase field approach that smears the crack over the whole domain of the body is employed in the same line with gradient damage formulations (Francfort and Marigo 1998; Bourdin et al. 2000; Forest 2009).

In the context of this approach, the dissipated surface energy can be approximated by a volume integral

$$\int_{\Gamma} \mathcal{G}_c\, \mathrm{d}\Gamma \approx \int_{\mathcal{B}_0} \mathcal{G}_c \gamma\left(\mathfrak{d}, \nabla_{\mathbf{X}}\mathfrak{d}\right)\, \mathrm{d}\Omega \tag{3}$$

where $\gamma\left(\mathfrak{d}, \nabla_{\mathbf{X}}\mathfrak{d}\right)$ is the crack surface density per unit volume, and $\nabla_{\mathbf{X}}\mathfrak{d}$ is the gradient of phase field variable. In this way, the sharp crack is regularized over the body inducing the diffusive representation, as shown in Fig. 2. The crack surface density $\gamma\left(\mathfrak{d}, \nabla_{\mathbf{X}}\mathfrak{d}\right)$ is defined according to the modified Ambrosio-Tortorelli functional (Gültekin et al. 2018)

$$\gamma\left(\mathfrak{d}, \nabla_{\mathbf{X}}\mathfrak{d}, \boldsymbol{\omega}\right) = \frac{1}{2l}\mathfrak{d}^2 + \frac{l}{2}\boldsymbol{\omega} : \left(\nabla_{\mathbf{X}}\mathfrak{d} \otimes \nabla_{\mathbf{X}}\mathfrak{d}\right) \tag{4}$$

where $\boldsymbol{\omega}$ is the second order structural tensor characterising the material anisotropy. In order to make the energy release rate orientation-dependent (Clayton and Knap 2015; Nguyen et al. 2017), the structural tensor can be defined as

$$\boldsymbol{\omega} = \mathbb{I}_2 + \alpha_p(\mathbb{I}_2 - \mathbf{N}_p \otimes \mathbf{N}_p) \tag{5}$$

where $\mathbb{I}_2$ is the second-order identity tensor, $\mathbf{N}_p$ represents the unit vector normal to the preferential cleavage plane, and α_p is the penalty parameter that is used to prevent damage to develop on planes not normal to $\mathbf{N}_p$. According to the previous study (Clayton and Knap 2014), this parameter should be greater than 1.0, and in case of isotropic material, the value is equal to 0.0.

The specific elastic energy Ψ is influenced by the phase field variable $\mathfrak{d}$, which is motivated by the fact that this energy in the damage transition zone has to decrease so as to ensure the thermodynamic equilibrium. Furthermore, to avoid the asymmetric damage behaviour, the elastic energy density can be split into the active contribution Ψ_+ and the passive contribution Ψ_- (Miehe et al. 2010b). During the reversal loading process, the crack closing precludes the damage evolution, and also provokes the stiffness discovery (Cavuoto

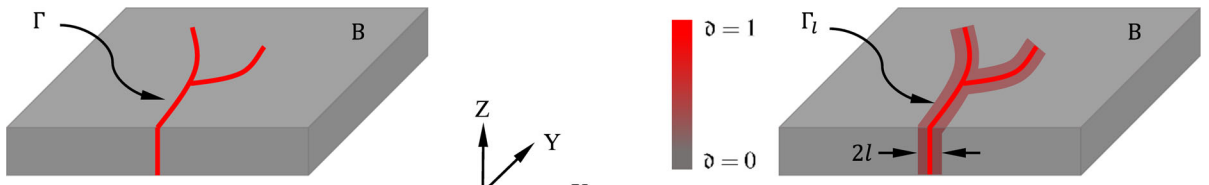

(a) Sharp crack topology (b) Diffusive crack topology

Fig. 2 Schematic diagram of solid body with (a) sharp crack topology, and (b) diffusive crack topology

et al. 2022). Based on the aforementioned viewpoints, the elastic energy Ψ can be defined as

$$\Psi = \mathfrak{g}(\mathfrak{d})\Psi_+ + \Psi_- \tag{6}$$

where $\mathfrak{g}(\mathfrak{d}) = (1-\mathfrak{d})^2 + \mathcal{K}$ denotes the monotonic degradation function, $\mathcal{K} \approx 0$ is a positive parameter to ensure numerical stability in case of fully material degradation, and is set to 1.0e−7 in this work.

2.2 Solid shell kinematics

In the concept of solid shell theory, the position vectors $\mathbf{X}$ and $\mathbf{x}$ in the reference and current configurations, and the phase field variable $\mathfrak{d}$ at any material point can be approximated by the corresponding vectors on the bottom and top surfaces of solid-like shell element, and can be defined as

$$\mathbf{X}\left(\xi^1,\xi^2,\xi^3\right) = \frac{1}{2}\left(1+\xi^3\right)\mathbf{X}_t\left(\xi^1,\xi^2\right) + \frac{1}{2}\left(1-\xi^3\right)\mathbf{X}_b\left(\xi^1,\xi^2\right) \tag{7a}$$

$$\mathbf{x}\left(\xi^1,\xi^2,\xi^3\right) = \frac{1}{2}\left(1+\xi^3\right)\mathbf{x}_t\left(\xi^1,\xi^2\right) + \frac{1}{2}\left(1-\xi^3\right)\mathbf{x}_b\left(\xi^1,\xi^2\right) \tag{7b}$$

$$\mathfrak{d}\left(\xi^1,\xi^2,\xi^3\right) = \frac{1}{2}\left(1+\xi^3\right)\mathfrak{d}_t\left(\xi^1,\xi^2\right) + \frac{1}{2}\left(1-\xi^3\right)\mathfrak{d}_b\left(\xi^1,\xi^2\right) \tag{7c}$$

where the parametric space is identified as: $\mathcal{A} := \left\{\xi = \left(\xi^1,\xi^2,\xi^3\right) \in \mathbb{R}^3 \mid -1 \le \xi^i \le +1; i = 1,2,3\right\}$, the subscript b and t represent bottom and top surfaces, respectively, and $\left(\xi^1,\xi^2,\xi^3\right)$ represent the coordinates in the parametric space.

The kinematics of solid shell element can be described by the use of the convective curvilinear system so that the ANS interpolation for the transverse normal and shear strain components can be implemented. The covariant tangent vectors $\mathbf{G}_i(\boldsymbol{\xi})$ and $\mathbf{g}_i(\boldsymbol{\xi})$ in the reference and current configuration are defined as the partial derivatives of corresponding position vectors $\mathbf{X}$ and $\mathbf{x}$ with respect to the convective coordinates ξ^i

$$\mathbf{G}_i(\boldsymbol{\xi}) := \frac{\partial \mathbf{X}(\boldsymbol{\xi})}{\partial \xi^i}, \quad \mathbf{g}_i(\boldsymbol{\xi}) := \frac{\partial \mathbf{x}(\boldsymbol{\xi})}{\partial \xi^i}, \quad i = 1,2,3 \tag{8}$$

The contravariant basis vectors can be determined in a standard manner by $\mathbf{G}_i \cdot \mathbf{G}^j = \delta_i^j$ and $\mathbf{g}_i \cdot \mathbf{g}^j = \delta_i^j$, and metric tensors are defined as $\mathbf{G} = G_{ij}\mathbf{G}^i \otimes \mathbf{G}^j = G^{ij}\mathbf{G}_i \otimes \mathbf{G}_j$, $\mathbf{g} = g_{ij}\mathbf{g}^i \otimes \mathbf{g}^j = g^{ij}\mathbf{g}_i \otimes \mathbf{g}_j$.

In curvilinear setting, the deformation gradient $\mathbf{F}^u$ is given by

$$\mathbf{F}^u = \frac{\partial \mathbf{x}}{\partial \mathbf{X}} = \mathbf{g}_i \otimes \mathbf{G}^i \tag{9}$$

where the Einstein summation convention on repeated indices is adopted here. Through the definition of metric tensor components $G_{ij} = \mathbf{G}_i \cdot \mathbf{G}_j$ and $g_{ij} = \mathbf{g}_i \cdot \mathbf{g}_j$ in the reference and current configuration, the displacement derived Green-Lagrange strain tensor is defined as

$$\mathbf{E}^u := \frac{1}{2}\left[\left(\mathbf{F}^u\right)^{\mathrm{T}}\mathbf{F}^u - \mathbb{I}_2\right] = \frac{1}{2}\left[g_{ij} - G_{ij}\right]\mathbf{G}^i \otimes \mathbf{G}^j \tag{10}$$

The energetically conjugated second Piola-Kirchhoff stress tensor is defined as

$$\mathbf{S} = S^{ij}\mathbf{G}_i \otimes \mathbf{G}_j \tag{11}$$

where S^{ij} represents the contravariant component.

3 Numerical implementation

In this section, the numerical strategy rooted in the use of finite element method for the spatial approximation is described briefly. Since this work is restricted to quasi-static analysis, no temporal integration scheme is required, which leads to an equilibrium problem at

each pseudo-time step. Firstly, the variational formulation and finite element interpolations are derived in Sect. 3.1. More specific details regarding the discretizations are ignored here for brevity, but can be found in the previous work (Liu et al. 2022). Secondly, the solution schemes proposed for the phase field solid shell formulation are depicted in Sect. 3.2.

3.1 Finite element interpolation

The mixed Hu-Washizu variational principle is adopted for the derivation of phase field solid shell formulation incorporating the Enhanced Assumed Strain (EAS) and Assumed Natural Strain (ANS) methods to alleviate the locking pathologies. It should be pointed out that the EAS method is employed to remedy volumetric and Poisson thickness locking, while the membrane and in-plane locking effects are tackled by the ANS method (Simo and Rifai 1990; Dvorkin and Bathe 1984). Given the enhancement based on the EAS method at finite deformation, the Green-Lagrange strain consists of two parts following the approach proposed in Bischoff and Ramm (1997), including the displacement derived compatible strain $\mathbf{E}^u$ and incompatible strain $\tilde{\mathbf{E}}$, and its complete form reads: $\mathbf{E} = \mathbf{E}^u + \tilde{\mathbf{E}}$.

The multi-field variational functional of the solid body takes the form of

$$\Pi(\mathbf{S}, \tilde{\mathbf{E}}, \mathbf{u}, \mathfrak{d}) = \int_{\mathcal{B}_0} \Psi\left(\mathbf{E}^u, \tilde{\mathbf{E}}, \mathfrak{d}\right) \mathrm{d}\Omega + \int_{\mathcal{B}_0} \frac{\mathcal{G}_c l}{2}\left[\frac{\mathfrak{d}^2}{l^2} + \boldsymbol{\omega} : (\nabla_{\mathbf{X}}\mathfrak{d} \otimes \nabla_{\mathbf{X}}\delta\mathfrak{d})\right] \mathrm{d}\Omega - \Pi_{\text{ext}} \quad ss \tag{12}$$

where Π_{ext} identifies the external energy functional. Note that the displacement $\mathbf{u}$, the phase field variable $\mathfrak{d}$, and the imcompatible strain $\tilde{\mathbf{E}}$ are the independent variables. Given the orthogonality condition between the stress and strain fields, the stress field is ignored in line with the previous work (Simo and Armero 1992). The first variation of Eq. (12) with respect to the independent fields is given by

$$\mathcal{R}^u(\mathbf{u}, \delta\mathbf{u}, \tilde{\mathbf{E}}, \mathfrak{d}) = \int_{\mathcal{B}_0} \frac{\partial \Psi}{\partial \mathbf{E}} : \frac{\partial \mathbf{E}^u}{\partial \mathbf{u}} \delta\mathbf{u} \mathrm{d}\Omega - \delta\Pi_{\text{ext}}(\mathbf{u}) = 0, \forall \delta\mathbf{u} \in \mathfrak{V}^u \tag{13a}$$

$$\mathcal{R}^{\tilde{E}}(\mathbf{u}, \tilde{\mathbf{E}}, \delta\tilde{\mathbf{E}}, \mathfrak{d}) = \int_{\mathcal{B}_0} \frac{\partial \Psi}{\partial \mathbf{E}} : \delta\tilde{\mathbf{E}}\, \mathrm{d}\Omega = 0, \forall \delta\tilde{\mathbf{E}} \in \mathfrak{V}^{\tilde{E}} \tag{13b}$$

$$\mathcal{R}^{\mathfrak{d}}(\mathbf{u}, \tilde{\mathbf{E}}, \mathfrak{o}, \delta\mathfrak{d}) = \int_{\mathcal{B}_0} -2(1-\mathfrak{d})\delta\mathfrak{d}\Psi_+ \mathrm{d}\Omega + \int_{\mathcal{B}_0} \mathcal{G}_c l\left[\frac{1}{l^2}\mathfrak{d}\delta\mathfrak{d} + \boldsymbol{\omega} : (\nabla_{\mathbf{X}}\mathfrak{d} \otimes \nabla_{\mathbf{X}}\delta\mathfrak{d})\right] \mathrm{d}\Omega = 0, \quad \forall \delta\mathfrak{d} \in \mathfrak{V}^{\mathfrak{d}} \tag{13c}$$

where $\mathfrak{V}^u$, $\mathfrak{V}^{\tilde{\mathbf{E}}}$ and $\mathfrak{V}^{\mathfrak{d}}$ are the admissible spaces of independent variables.

According to the concept of isoparametric interpolation, the position vectors $\mathbf{X}$ and $\mathbf{x}$ in the reference and current configurations, the displacement vector $\mathbf{u}$ and its variation $\delta\mathbf{u}$, and the phase field variable $\mathfrak{d}$ and its variation $\delta\mathfrak{d}$ can be approximated by

$$\mathbf{X} = \mathbf{N}\tilde{\mathbf{X}}, \quad \mathbf{x} = \mathbf{N}\tilde{\mathbf{x}} \tag{14a}$$

$$\mathbf{u} = \mathbf{N}\mathbf{d}, \quad \delta\mathbf{u} = \mathbf{N}\delta\mathbf{d} \tag{14b}$$

$$\mathfrak{d} = \mathbf{N}^{\mathfrak{d}}\bar{\mathfrak{d}}, \quad \delta\mathfrak{d} = \mathbf{N}^{\mathfrak{d}}\delta\bar{\mathfrak{d}} \tag{14c}$$

where $\tilde{\mathbf{X}}$ and $\tilde{\mathbf{x}}$ are the corresponding nodal position vectors, $\mathbf{d}$ denotes the nodal displacement vector, and $\bar{\mathfrak{d}}$ represents the nodal phase field vector. The shape function matrix $\mathbf{N}^{\mathfrak{d}}$ is defined as

$$\mathbf{N}^{\mathfrak{d}} = [\mathrm{N}_1,\ \mathrm{N}_2,\ \mathrm{N}_3,\ \mathrm{N}_4,\ \mathrm{N}_5,\ \mathrm{N}_6,\ \mathrm{N}_7,\ \mathrm{N}_8] \tag{15}$$

where its component N_{I} is given by

$$\mathrm{N}_{\mathrm{I}} = \frac{1}{8}\left(1 + \xi_{\mathrm{I}}^1\xi^1\right)\left(1 + \xi_{\mathrm{I}}^2\xi^2\right)\left(1 + \xi_{\mathrm{I}}^3\xi^3\right) \tag{16}$$

with $\xi_{\mathrm{I}}^1, \xi_{\mathrm{I}}^2, \xi_{\mathrm{I}}^3 = \pm 1$. The material gradient of phase field $\nabla_{\mathbf{X}}\mathfrak{d}$ and its variation $\nabla_{\mathbf{X}}\delta\mathfrak{d}$ can be defined as

$$\nabla_{\mathbf{X}}\mathfrak{d} = \mathbf{G}^{-\mathrm{T}}\nabla_{\boldsymbol{\xi}}\bar{\mathfrak{d}} = \mathbf{B}^{\mathfrak{d}}(\boldsymbol{\xi})\bar{\mathfrak{d}}, \quad \nabla_{\mathbf{X}}\delta\mathfrak{d} = \mathbf{G}^{-\mathrm{T}}\nabla_{\boldsymbol{\xi}}\delta\bar{\mathfrak{d}} = \mathbf{B}^{\mathfrak{d}}(\boldsymbol{\xi})\delta\bar{\mathfrak{d}} \tag{17}$$

where $\nabla_{\boldsymbol{\xi}}$ denotes the gradient with respect to the natural coordinates.

The vector form of the Green-Lagrange strain tensor is given by $\mathbf{E} = [\mathrm{E}_{11}, 2\mathrm{E}_{12}, 2\mathrm{E}_{13}, \mathrm{E}_{22}, 2\mathrm{E}_{23}, \mathrm{E}_{33}]^{\mathrm{T}}$. To alleviate the curvature thickness locking effects, the ANS method proposed in Betsch and Stein (1995) is adopted to modify the transverse normal strain component E_{33} by four collocation points defined in convective coordinates ξ_{C_i} as $\xi_{\mathrm{C}_1} = (-1, -1, 0)$, $\xi_{\mathrm{C}_2} = (1, -1, 0)$, $\xi_{\mathrm{C}_3} = (1, 1, 0)$, and $\xi_{\mathrm{C}_4} = (-1, 1, 0)$, see Fig. 3. Besides, to prevent transverse shear locking, the ANS method proposed in Dvorkin and Bathe (1984) is also employed in this work. The four collocation points for the enhancement of transverse shear strain components are $\xi_{\mathrm{A}_1} = (0, -1, 0)$, $\xi_{\mathrm{A}_2} = (0, 1, 0)$, $\xi_{\mathrm{B}_1} = (-1, 0, 0)$, and $\xi_{\mathrm{B}_2} = (1, 0, 0)$, see Fig. 3. Given

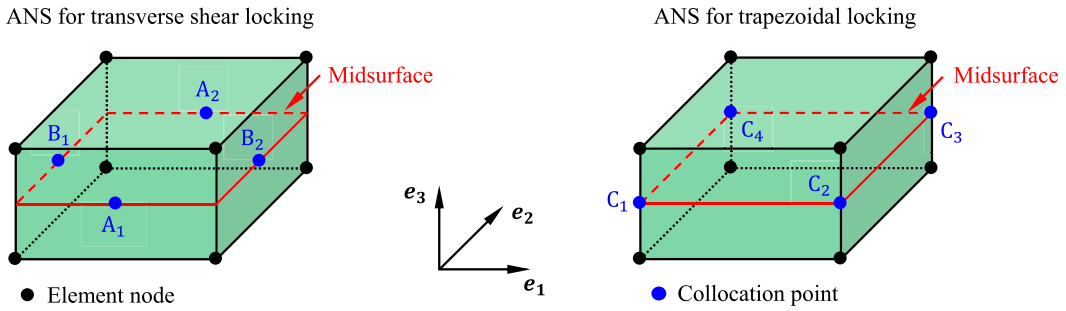

Fig. 3 Position of collocation points in the element parametric space for the ANS method

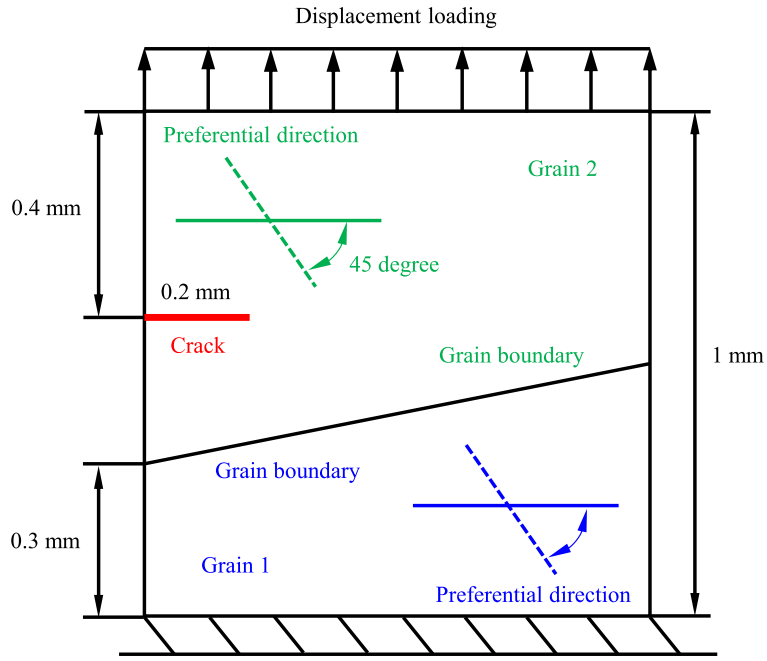

Fig. 4 Schematic of the benchmark problem for anisotropic fracture modeling

the aforementioned ANS interpolations, the strain vector is given by

$$\mathbf{E}^u = \begin{bmatrix} \frac{1}{2}\left(g_{11} - G_{11}\right) \\ \left(g_{12} - G_{12}\right) \\ \left(1-\xi^2\right)\left(g_{13}^{\mathrm{A}_1} - G_{13}^{\mathrm{A}_1}\right) + \left(1+\xi^2\right)\left(g_{13}^{\mathrm{A}_2} - G_{13}^{\mathrm{A}_2}\right) \\ \frac{1}{2}\left(g_{22} - G_{22}\right) \\ \left(1-\xi^1\right)\left(g_{23}^{\mathrm{B}_1} - G_{23}^{\mathrm{B}_1}\right) + \left(1+\xi^1\right)\left(g_{23}^{\mathrm{B}_2} - G_{23}^{\mathrm{B}_2}\right) \\ \sum_{i=1}^{4} \frac{1}{4}\left(1+\xi_i^1\xi^1\right)\left(1+\xi_i^2\xi^2\right)\frac{1}{2}\left(g_{33}^{\mathrm{C}_i} - G_{33}^{\mathrm{C}_i}\right) \end{bmatrix} \tag{18}$$

where the superscripts A_1, A_2, B_1, B_2, and C_i with $i = 1, 2, 3, 4$ stand for the corresponding collocation points. The approximation of virtual strain is given by

$$\delta\mathbf{E}^u = \mathbf{B}\delta\mathbf{d} \quad \text{with } \mathbf{B} = [\mathbf{B}_1, \mathbf{B}_2, \mathbf{B}_3, \mathbf{B}_4, \mathbf{B}_5, \mathbf{B}_6, \mathbf{B}_7, \mathbf{B}_8] \tag{19}$$

where $\mathbf{B}_\mathrm{I}$ is the interpolation matrix for each node I. According to the previous work (Klinkel and Wagner 1997; Vu-Quoc and Tan 2003), the interpolations of incompatible strain vector $\tilde{\mathbf{E}}$ and its variation $\delta\tilde{\mathbf{E}}$ are given by

$$\tilde{\mathbf{E}} \approx \mathbf{M}(\xi)\boldsymbol{\zeta}, \quad \delta\tilde{\mathbf{E}} \approx \mathbf{M}(\xi)\delta\boldsymbol{\zeta} \tag{20}$$

where $\mathbf{M}(\xi)$ is the interpolation matrix of the enhancing modes $\boldsymbol{\zeta}$, and is defined as

$$\mathbf{M}(\xi) = \left[\frac{\det \mathbf{J}_0}{\det \mathbf{J}}\right] \mathbf{T}_0^{-\mathrm{T}} \tilde{\mathbf{M}}(\xi) \tag{21}$$

where $\mathbf{J} = [\mathbf{G}_1, \mathbf{G}_2, \mathbf{G}_3]^\mathrm{T}$, $\mathbf{J}_0$ is its evaluation at the element center, $\mathbf{T}_0$ is the tranformation matrix, and $\tilde{\mathbf{M}}(\xi)$ is the interpolation matrix in the parametric space (Liu et al. 2022).

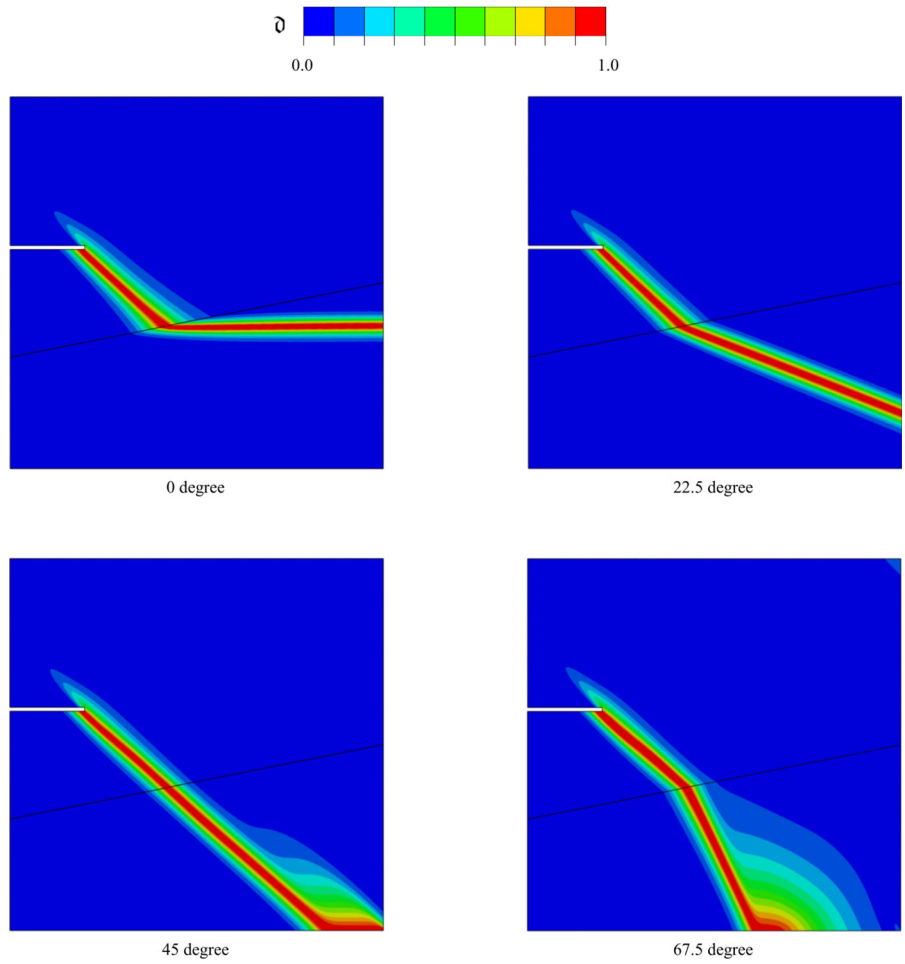

Fig. 5 The phase field contour plots of fully cracked specimen with the preferential crack orientation of Grain 1 equal to 0 degree, 22.5 degree, 45 degree, and 67.5 degree

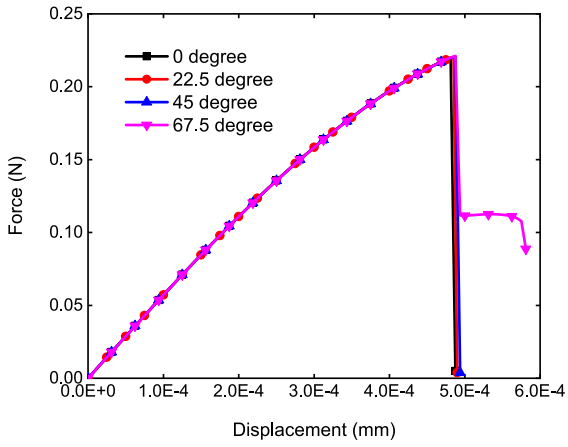

Fig. 6 The obtained force vs. displacement curves with the preferential crack orientation of Grain 1 equal to 0 degree, 22.5 degree, 45 degree, and 67.5 degree

Inserting the aforementioned interpolations into Eqs. (13), the discretes residual equations are given by

$$\mathbf{R}^{d}(\mathbf{d},\delta\mathbf{d},\bar{\mathfrak{d}},\boldsymbol{\zeta}) = \int_{\mathcal{B}_0} \mathfrak{g}(\mathfrak{d})\mathbf{B}(\mathbf{d})^{\mathrm{T}}\mathbf{S}\,\mathrm{d}\Omega - \mathbf{R}^{d}_{\mathrm{ext}} \tag{22a}$$

$$\mathbf{R}^{\zeta}(\mathbf{d},\bar{\mathfrak{d}},\boldsymbol{\zeta},\delta\boldsymbol{\zeta}) = \int_{\mathcal{B}_0} \mathfrak{g}(\mathfrak{d})\mathbf{M}(\boldsymbol{\xi})^{\mathrm{T}}\mathbf{S}\,\mathrm{d}\Omega \tag{22b}$$

$$\mathbf{R}^{\mathfrak{d}}(\mathbf{d},\bar{\mathfrak{d}},\delta\bar{\mathfrak{d}},\boldsymbol{\zeta}) = \int_{\mathcal{B}_0} -2(1-\mathfrak{d})\mathbf{N}(\boldsymbol{\xi})^{\mathrm{T}}\Psi_{+}\mathrm{d}\Omega + \int_{\mathcal{B}_0} \mathcal{G}_c l\left[\left(\mathbf{B}^{\mathfrak{d}}\right)^{\mathrm{T}}\mathbf{W}\nabla_{\mathbf{X}}\mathfrak{d} + \frac{1}{l^2}\mathbf{N}(\boldsymbol{\xi})^{\mathrm{T}}\mathfrak{d}\right]\mathrm{d}\Omega \tag{22c}$$

To avoid the irreversible growth of the fracture process, a history variable H is introduced to modify the residual vector $\mathbf{R}^{\mathfrak{d}}$ (Msekh et al. 2015), which is transformed into

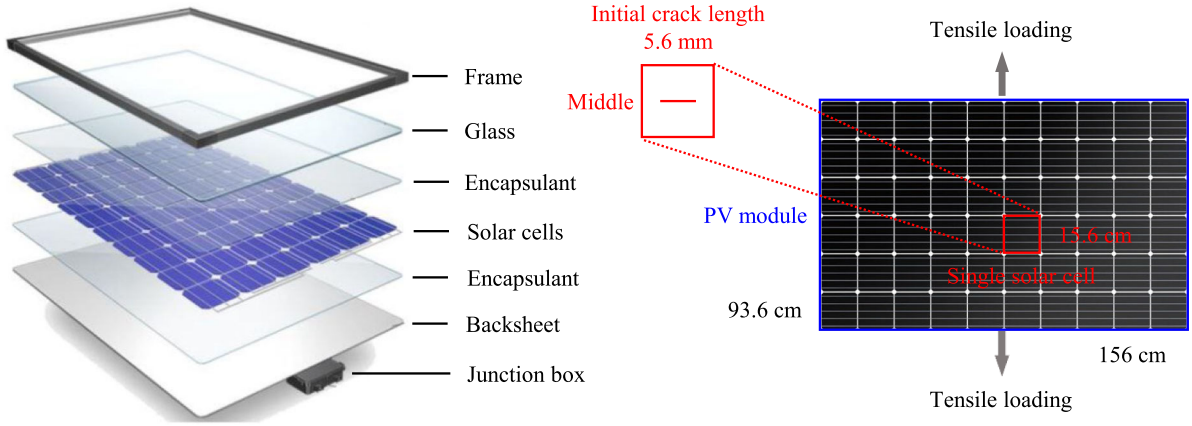

Fig. 7 Schematic diagram of the local fracture modeling of one single solar cell when the photovoltaic module is subjected to tensile loading

$$\mathbf{R}^{\mathfrak{d}} = \int_{\mathcal{B}_0} -2(1-\mathfrak{d})\mathbf{N}(\boldsymbol{\xi})^{\mathrm{T}} H \mathrm{d}\Omega + \int_{\mathcal{B}_0} \mathcal{G}_c l \left[\left(\mathbf{B}^{\mathfrak{d}}\right)^{\mathrm{T}} \mathbf{W} \nabla_{\mathbf{X}} \mathfrak{d} + \frac{1}{l^2} \mathbf{N}(\boldsymbol{\xi})^{\mathrm{T}} \mathfrak{d} \right] \mathrm{d}\Omega \tag{23}$$

In view of the irrevisibility (Miehe et al. 2010b), the history variable H must obey the following Kuhn-Tucker conditions

$$\Psi_+ - H \leqslant 0, \quad \dot{H} \geqslant 0, \quad \dot{H}\left(\Psi_+ - H\right) = 0 \tag{24}$$

At the certain time point t, the history variable H can be expressed as

$$H = \max_{\tau \in [0,t]} \Psi_+(\tau) \tag{25}$$

To solve the multi-field problem, an iterative scheme is adopted, and the consistent linearization of Eqs. (22) obtained from the concept of Gateaux directional derivative can be derived as

$$\begin{bmatrix} \mathbf{k}_{dd} & \mathbf{k}_{d\zeta} & \mathbf{0} \\ \mathbf{k}_{\zeta d} & \mathbf{k}_{\zeta\zeta} & \mathbf{0} \\ \mathbf{0} & \mathbf{0} & \mathbf{k}_{\mathfrak{d}\mathfrak{d}} \end{bmatrix} \begin{bmatrix} \Delta \mathbf{d} \\ \Delta \boldsymbol{\zeta} \\ \Delta \bar{\mathfrak{d}} \end{bmatrix} = \begin{bmatrix} \mathbf{R}^d_{\mathrm{ext}} \\ \mathbf{0} \\ \mathbf{0} \end{bmatrix} - \begin{bmatrix} \mathbf{R}^d \\ \mathbf{R}^{\zeta} \\ \mathbf{R}^{\mathfrak{d}} \end{bmatrix} \tag{26}$$

It is worth mentioning that the derivation of stiffness terms are omitted here for brevity, see (Liu et al. 2022). Since inter-element continuity of the enhanced strain field is not required, the second equation of Eqs. (26) can be condensed out in the element level in line with (Bischoff and Ramm 1997), and the condensed equations can be expressed as

$$\begin{bmatrix} \mathbf{k}^*_{dd} & \mathbf{0} \\ \mathbf{0} & \mathbf{k}_{\mathfrak{d}\mathfrak{d}} \end{bmatrix} \begin{bmatrix} \Delta \mathbf{d} \\ \Delta \bar{\mathfrak{d}} \end{bmatrix} = \begin{bmatrix} \mathbf{R}^d_{\mathrm{ext}} \\ \mathbf{0} \end{bmatrix} - \begin{bmatrix} \mathbf{R}^{d*} \\ \mathbf{R}^{\mathfrak{d}} \end{bmatrix} \tag{27}$$

Table 1 Mechanical properties for photovoltaic modules (Paggi et al. 2011; Corrado et al. 2017)

	E (GPa)	Density (kg/m^3)
Backsheet	2.8	1200
EVA	0.01	1180
Glass	73	2500

where the modified stiffness $\mathbf{k}^*_{dd}$ and residual vector $\mathbf{R}^{d*}$ are defined as

$$\mathbf{k}^*_{dd} = \mathbf{k}_{dd} - \mathbf{k}_{d\zeta}\mathbf{k}^{-1}_{\zeta\zeta}\mathbf{k}_{\zeta d} \tag{28a}$$

$$\mathbf{R}^{d*} = \mathbf{R}^d - \mathbf{k}_{d\zeta}\mathbf{k}^{-1}_{\zeta\zeta}\mathbf{R}^{\zeta} \tag{28b}$$

3.2 Solution schemes

In order to solve the nonlinear iterative equations, two different schemes are widely employed for the coupled phase field-displacement problem, including the monolithic and staggered schemes. Monolithic scheme retains unconditional stability, but suffers from poor convergence performance that hinders its wide application. On the other hand, the staggered scheme is very robust and can overcome the convergence issue. However, very small time increment must be adopted to prevent the solution deviating from the equilibrium, so this solution scheme is very time-consuming. In the following, the quasi-Newton monolithic scheme with improved performance in terms of both convergence and computational efficiency is introduced here for the

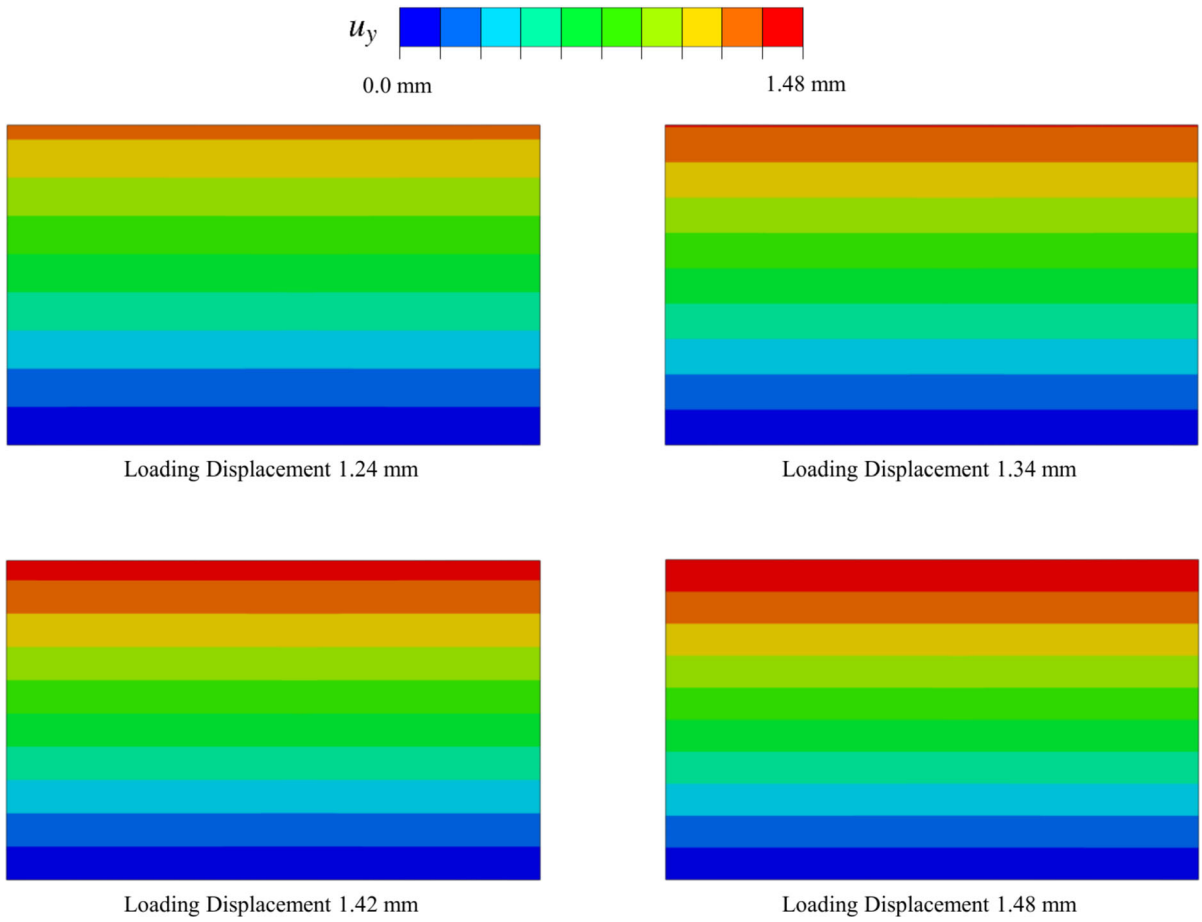

Fig. 8 The predicted displacement contour plots of the whole photovoltaic module when subjected to tensile loading at the loading displacement 1.24 mm, 1.34 mm, 1.42 mm, and 1.48 mm

solution of phase field problem using solid shell formulation.

Given the data $\{\mathbf{d}_n, \boldsymbol{\zeta}_n, \bar{\mathfrak{d}}_n\}$ at the previous converged increment t_n, the solution of the next increment $\left[t_n, t_{n+1}^{(k)}\right]$ requires iterations around the intermediate state $\{\mathbf{d}_{n+1}^{(k)}, \boldsymbol{\zeta}_{n+1}^{(k)}, \bar{\mathfrak{d}}_{n+1}^{(k)}\}$. According to the static condensation procedure in the previous section, the nodal phase field and displacement vectors are defined as unknowns at the element level, and the enhancing vector at the next time increment of iteration k, e.g. $\Delta\boldsymbol{\zeta}_{n+1}^{(k)}$, should be determined for the computational procedure. Based on the algorithm described in Reinoso and Blázquez (2016), the increment $\Delta\boldsymbol{\zeta}_{n+1}^{(k)}$ is given by

$$\Delta\boldsymbol{\zeta}_{n+1}^{(k)} = -\left[\mathbf{k}_{\zeta\zeta,n}\right]^{-1}\left[\mathbf{R}_{\mathrm{int},n}^{\zeta} + \mathbf{k}_{\zeta d,n}\Delta\mathbf{d}_{n+1}^{(k)}\right] \tag{29}$$

Note that the increments $\Delta\mathbf{d}_{n+1}^{(k)}$ and $\Delta\bar{\mathfrak{d}}_{n+1}^{(k)}$ are provided by the solver, while the element matrices at the previous increment $\left[\mathbf{k}_{\zeta\zeta,n}\right]^{-1}$, $\mathbf{R}_{\mathrm{int},n}^{\zeta}$, $\mathbf{k}_{\zeta d,n}$, and $\boldsymbol{\zeta}_n$ are all stored as internal variables.

In the quasi-Newton method, the stiffness will be updated only after a certain number of iterations without achieving convergence (Wu et al. 2020). Specifically, the approximated stiffness matrix must satisfy the following equation

$$\widetilde{\mathbf{K}}\delta\mathbf{z} = \delta\mathbf{R} \tag{30}$$

for the residual $\delta\mathbf{z} := \mathbf{z}_{t+\Delta t} - \mathbf{z}_t$, in which the vectors $\mathbf{z}$ and $\delta\mathbf{R}$ are defined as $\mathbf{z} = [\mathbf{d}, \bar{\mathfrak{d}}]^{\mathrm{T}}$ and $\delta\mathbf{R} := \mathbf{R}_{t+\Delta t} - \mathbf{R}_t$, respectively. The approximated stiffness $\widetilde{\mathbf{K}}$ can be determined by

$$\widetilde{\mathbf{K}} = \widetilde{\mathbf{K}}_t - \frac{\left(\widetilde{\mathbf{K}}_t\delta\mathbf{z}\right)\left(\widetilde{\mathbf{K}}_t\delta\mathbf{z}\right)^{\mathrm{T}}}{\delta\mathbf{z}^{\mathrm{T}}\widetilde{\mathbf{K}}_t\delta\mathbf{z}} + \frac{\delta\mathbf{R}\delta\mathbf{R}^{\mathrm{T}}}{\delta\mathbf{z}^{\mathrm{T}}\delta\mathbf{R}} \tag{31}$$

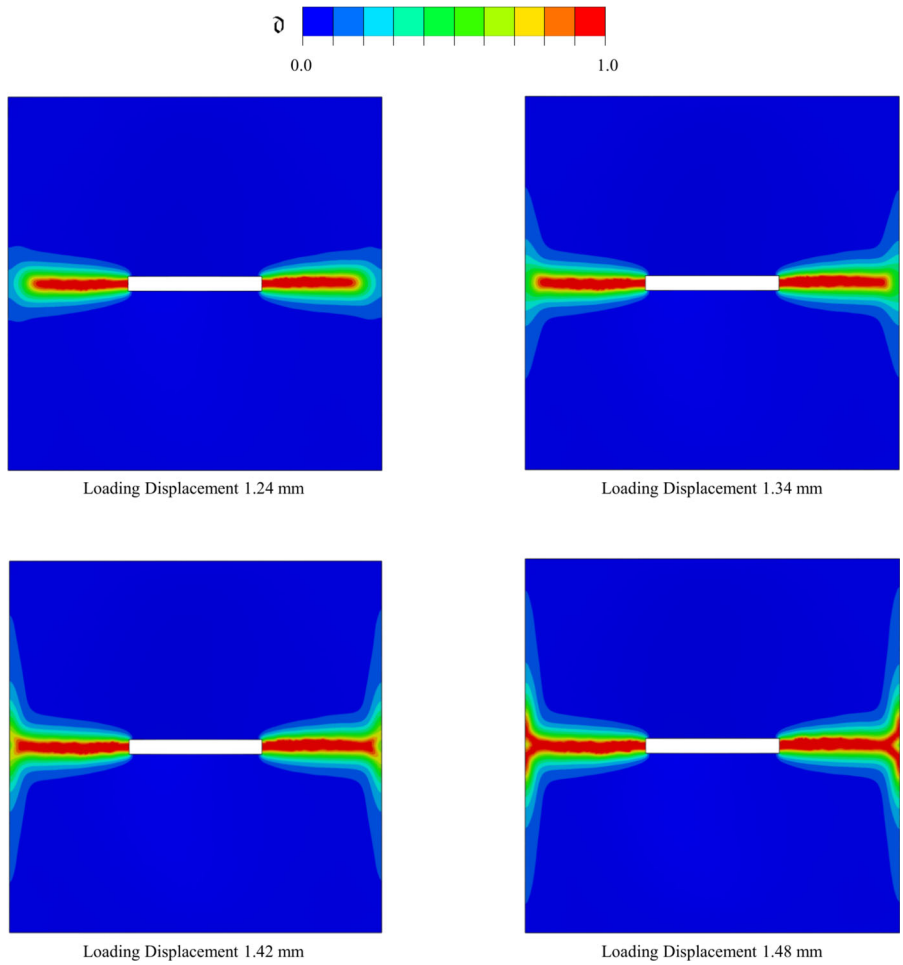

Fig. 9 The predicted phase field contour plots of the local model with no fracture anisotropy at the loading displacement 1.24 mm, 1.34 mm, 1.42 mm, and 1.48 mm

It is worth noting that the updated stiffness matrix in case of symmetry can be written as Matthies and Strang (1979)

$$\widetilde{\mathbf{K}}^{-1} = \left(\mathbf{I} - \frac{\delta\mathbf{z}\delta\mathbf{R}^{\mathrm{T}}}{\delta\mathbf{z}^{\mathrm{T}}\delta\mathbf{R}}\right)\widetilde{\mathbf{K}}_t^{-1}\left(\mathbf{I} - \frac{\delta\mathbf{z}\delta\mathbf{R}^{\mathrm{T}}}{\delta\mathbf{z}^{\mathrm{T}}\delta\mathbf{R}}\right)^{\mathrm{T}} + \frac{\delta\mathbf{z}\delta\mathbf{z}^{\mathrm{T}}}{\delta\mathbf{z}^{\mathrm{T}}\delta\mathbf{R}} \tag{32}$$

The initial guess of the stiffness $\widetilde{\mathbf{K}}^{(0)}$ is defined as

$$\widetilde{\mathbf{K}}^{(0)} = \begin{bmatrix} \mathbf{K}_{dd}^{*} & \mathbf{0} \\ \mathbf{0} & \mathbf{K}_{\partial\partial} \end{bmatrix} \tag{33}$$

The stiffness will be reformed whenever the number of iterations exceed 8 without achieving the required convergence.

4 Numerical examples

In this section, the capability of proposed modeling framework is demonstrated through different numerical examples regarding cracking events in silicon solar cells of photovoltaics. Firstly, the feasibility to model anisotropic fracture using the current approach is shown through a demonstration problem in Sect. 4.1. Then, the solar cell cracking modeling in the photovoltaic module under two different loading cases are presented in Sect. 4.2.

4.1 Benchmark example of anisotropic fracture

In this example, the model will be assessed through a benchmark problem consisting in a square specimen that contains two parts and an initial crack, as shown in Fig. 4. The size of the specimen is 1 mm, and the initial

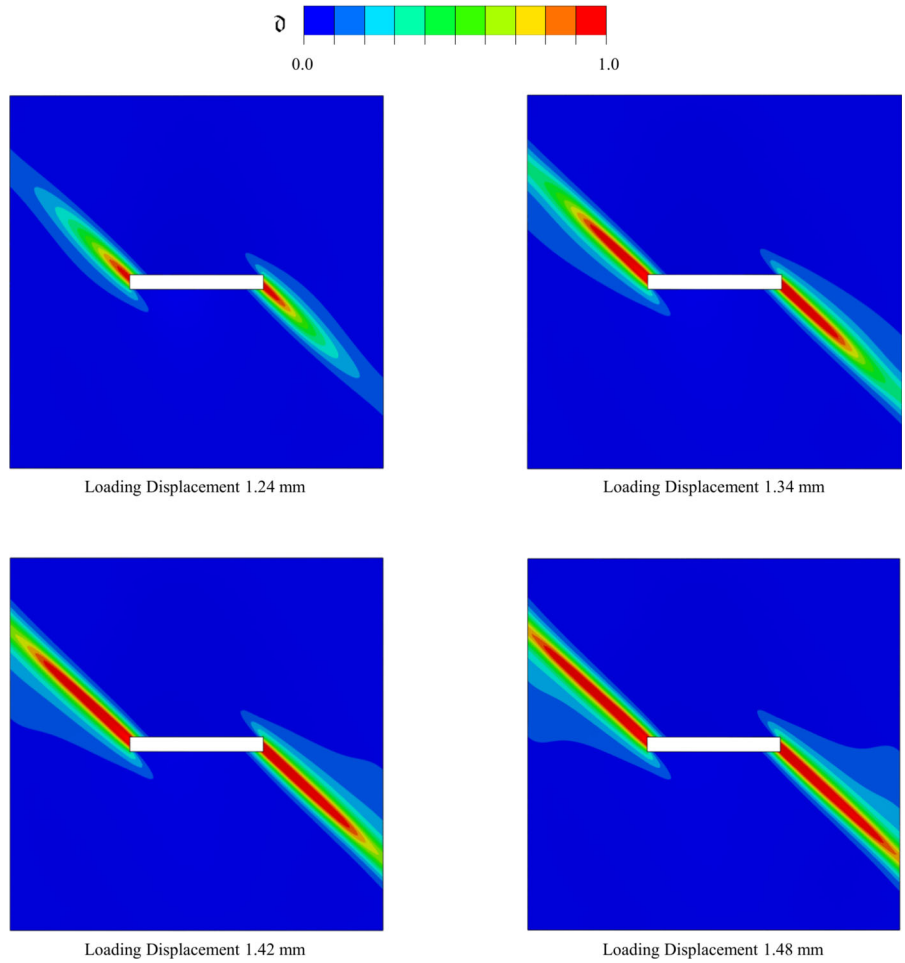

Fig. 10 The predicted phase field contour plots of the local model with the preferential crack orientation angle equal to 45 degree at the loading displacement of 1.24 mm, 1.34 mm, 1.42 mm, and 1.48 mm

crack length is 0.2 mm. The elastic modulus and critical fracture energy release rate are set to 160 GPa and 4.32 N/m, respectively, which are the typical material properties of silicon solar cells in photovoltaic modules (Paggi et al. 2018). The preferential crack plane of the Grain 2 with an initial crack is oriented with a fixed angle of 45 degree, while the preferential crack direction of the Grain 1 varies with respect to the horizontal axis of the whole domain. Regarding the boundary condition, the bottom facet is constrained in the vertical direction, and a tensile loading is applied to the upper facet of the specimen. The specimen is discretized using the solid shell elements, and the mesh size is 0.005 mm, which is approximately five times smaller than the phase field length scale. The total number of the elements in this numerical example is 46169. As mentioned before, α_p is the penalty parameter that should be greater than 1.0, and it is set to 10.0 in the simulation.

The predicted contour plots of phase field with different preferential crack orientations of Grain 1 are shown in Fig. 5. Different crack patterns can be observed with different preferential crack planes. The crack propagates from the initial crack following the fixed crack orientation through the domain of Grain 2, and when approaching the boundary between the two grains, crack deviation occurs due to the different nature of Grain 1. As shown in Fig. 5, the crack path through the Grain 1 when the specimen is fully cracked exactly follows the expected orientation. The force versus displacement curves for the different crack orientations of Grain 1 are plotted in Fig. 6. It can be seen that the crack preferential orientation of Grain 1 has negligible influence on the mechanical response. The approximate linear behaviour can be observed before

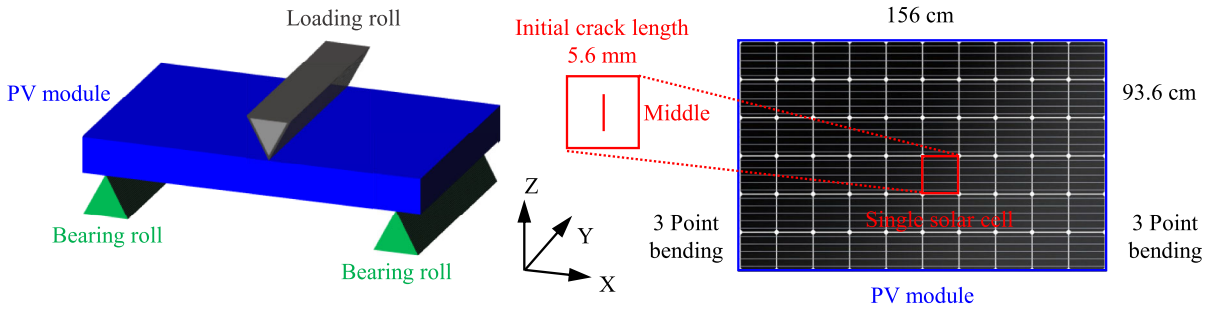

Fig. 11 Schematic diagram of the local fracture modeling of one single solar cell when the photovoltaic module is subjected to three point bending

the specimen is fully cracked when the loading displacement reaches around 0.0005 mm. After the peak values, all the curves drops down to zero immediately except the curve with crack orientation angle of Grain 1 equal to 67.5 degree, which can be ascribed to the fact that part of specimen is still constrained even when reaching the fully cracked state in this case. It should be pointed out that the different crack patterns can create different electrically inactive area in the silicon solar cell, leading to different power loss of the photovoltaic modules. Hence, the fracture anisotropy must be taken into account for the modeling of cracking events (Paggi et al. 2016).

4.2 Silicon solar cell cracking in the photovoltaic module

The modeling framework is further assessed in this section with application to the more realistic simulation of silicon solar cell cracking inside the photovoltaic module when subjected to the different external loadings. According to the experimental investigations (Sander et al. 2013; Paggi et al. 2016), the cracking events of silicon solar cells have negligible influence on the global stiffness of photovoltaic modules, and as a result, the global–local approach proposed in Liu et al. (2022) can be employed to reduce the computational cost by decoupling the elastic modeling of photovoltaic module with the fracture modeling of silicon solar cells. In this approach, the photovoltaic module is assumed to be purely elastic corresponding to the global model, and its solution at each time step is used to drive the local fracture modeling of silicon solar cell with the phase field approach. Hence, the global and local models are solved in a staggered manner, which features the one-way coupling in line with experimental evidence. The cracking events of one single silicon solar cell when the photovoltaic modules are subjected to two different loading cases are investigated to comprehensively showcase the capability of the modeling framework

In the first case, the tensile loading is applied to the photovoltaic module, and there is an initial notch perpendicular to the loading direction in the middle of one single solar cell, as shown in Fig. 7. The photovoltaic module is basically a thin-walled laminate structure that consists of different layers, including glass, backsheet, solar cells, and so on Liu et al. (2022). The material properties of photovoltaic modules are listed in Table 1, which are taken from Paggi et al. (2011), Corrado et al. (2017). The key component of the photovoltaic module is the silicon cell layer that converts the solar energy into electrical energy. It is very thin with the thickness of aproximately 0.1 mm (Liu et al. 2023), and can be broken easily due to the fragility. Each module contains 60 silicon solar cells, and the local crack propagation in the one single thin-film solar cell can be modeled by the phase field approach using solid shell formulation. The initial crack in the single solar cell is vertical to the tensile loading direction, and its length is 56 mm. The phase field length scale is set to 3 mm, and the mesh size is set to 1 mm. The predicted contour plots of displacement in the module at the loading displacement 1.24 mm, 1.34 mm, 1.42 mm, and 1.48 mm are shown in Fig. 8. At each time step, the global solution is used to drive the crack propagation of local model with uniform fine mesh by interpolation (Liu et al. 2022). Hence, the boundary condition of the local model is determined by the global solution at each time step. Due to fracture anisotropy, the local model can have different crack paths. In case of isotropic fracture,

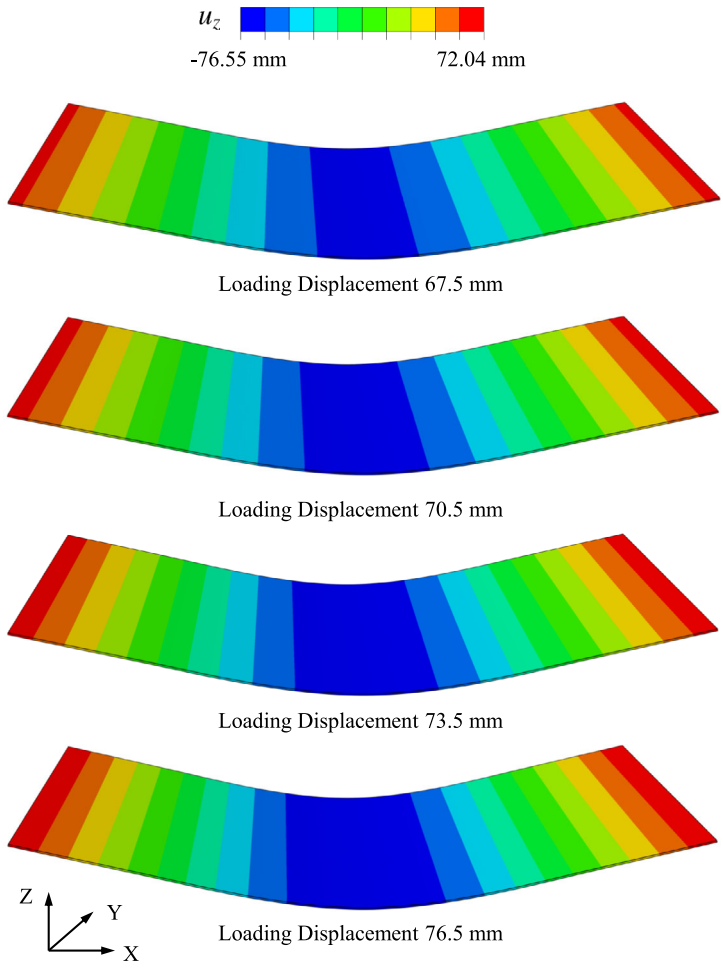

Fig. 12 The predicted displacement contour plots of the whole photovoltaic module when subjected to three point bending at the loading displacement 67.5 mm, 70.5 mm, 73.5 mm, and 76.5 mm

the phase field contour plots of the local model corresponding to the four loading stages are shown in Fig. 9. On the other hand, when the preferential crack orientation angle is set to 45 degree, the crack growth can be observed from Fig. 10.

In the second example, the three point bending is simulated, and its schematic is shown in Fig. 11. During the service lifetime in the outdoor environment, the photovoltaic modules can be subjected to different environmental loadings from wind, snow, hail impact and so on. It should be pointed out that in these cases the resulting bending mode frequently occurs, which will lead to the cracking of silicon solar cell inside the photovoltaic modules. Hence, the numerical example here could be of great practical interest from the photovoltaic industry. In this example, the bottom of the photovoltaic module is supported by two bearing rolls, and the vertical loading will be applied to the upper of the module by the loading roll, as shown in Fig. 11. The initial crack in the single solar cell is parallel to the loading roll in the middle location, and its length is 56 mm. The global photovoltaic module is meshed with element size of 6 mm, while the mesh size of the very refined local solar cell is 1 mm, which is three times smaller than the phase field length scale. The predicted displacement contour plots of the module along the loading direction at four loading stages are shown in Fig. 12. It can be seen that the deformation at the middle area of the photovoltaic module is very large as expected, which will lead to the crack growth of the local solar cell in this area. The local model driven by the global solution at each time step should have mixed boundary conditions in this case, including both pure bending and tension. Figure 13 shows the phase field contour plots of the local model with no fracture anisotropy at four different loading stages, while Fig. 14 indicates the phase

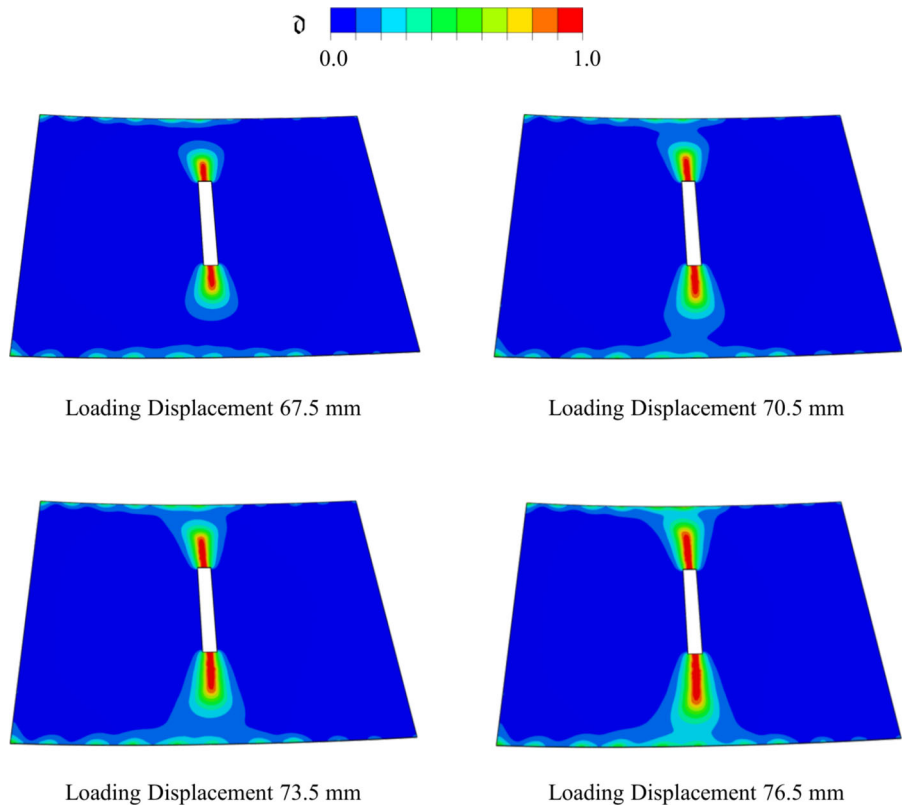

Fig. 13 The predicted phase field contour plots of the local model with no fracture anisotropy at the loading displacement 67.5 mm, 70.5 mm, 73.5 mm, and 76.5 mm

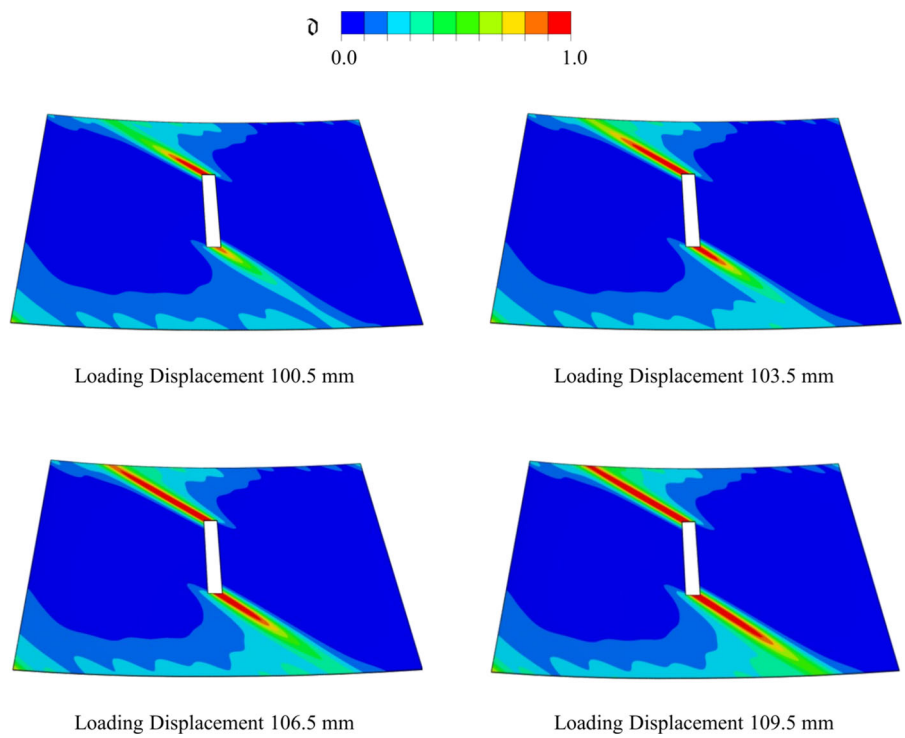

Fig. 14 The predicted phase field contour plots of the local model with the preferential crack orientation angle equal to 45 degree at the loading displacement 100.5 mm, 103.5 mm, 106.5 mm, and 109.5 mm

field contour plots of the local model with the preferential crack orientation angle equal to 45 degree, which presents completely different crack patterns compared to the former. Note that when the preferential crack orientation is set to 0 degree, the silicon solar cell is fully cracked when the loading displacement imposed on the global photovoltaic module reaches 76.5 mm, while in the case with the preferential crack orientation equal to 45 degree, the silicon solar cell is not fully cracked until when the loading displacement reaches 109.5 mm. It can be concluded here that the orientation of silicon cell will significantly influence the crack growth when the photovoltaic module is subjected to bending loading, which could provide guidance to the photovoltaic industry for the better design of photovoltaic products with excellent crack-resistant performance.

5 Concluding remarks

The present modeling strategy constitutes a major progress with respect to the state of the art, since it provides the first proof of concept of a computational methodology integrating structural mechanics considerations for real photovoltaic installations and advanced fracture mechanics models for the assessment of damage distributions in solar cells. To accurately capture the structural deformation of very thin silicon solar cells, the solid shell element is formulated at large deformation, which is incorporated into the phase field approach for the cracking modeling using the efficient and robust quasi-Newton solution. Note that the fracture anisotropy is also taken into account in the phase field solid shell formulation so that experimental crack patterns with varying orientation can be reproduced. For the sake of reducing computational cost of phase field fracture modeling, a global local approach suitable for the local fracture modeling of solar cells in the global level of photovoltaic module is explored, which is demonstrated by the simulation of several different loading cases. Given the complexity of loading scenarios of photovoltaic modules in the outdoor environment, this global local fracture modeling method can be very promising for the possible realistic prediction of crack growth of silicon solar cells.

Acknowledgements This paper is dedicated to the memory of Prof. Dominique Leguillon, who was a close friend and an extraordinary researcher

Funding Funding for open access publishing: Universidad de Sevilla/CBUA The authors acknowledge funding received from the European Union's H2020-MSCA-ITN-2019 research and innovation program under the Marie Skłodowska-Curie grant agreement no. 861061 - Project NEWFRAC "New strategies for multifield fracture problems across scales in heterogeneous systems for Energy, Health and Transport". J. Reinoso acknowledges the support of Ministerio de Ciencia e Innovación de España through the Project TED2021-131649B-I00

Data Availability No datasets were generated or analysed during the current study.

Declarations

Conflict of interest The authors declare no conflict of interest.

References

Ambati M, De Lorenzis L (2016) Phase-field modeling of brittle and ductile fracture in shells with isogeometric NURBS-based solid-shell elements. Comput Methods Appl Mech Eng 312:351–373

Ambati M, Gerasimov T, De Lorenzis L (2015) Phase-field modeling of ductile fracture. Comput Mech 55:1017–1040

Amiri F, Millán D, Shen Y, Rabczuk T, Arroyo M (2014) Phase-field modeling of fracture in linear thin shells. Theoret Appl Fract Mech 69:102–109

Areias P, Rabczuk T, Msekh M (2016) Phase-field analysis of finite-strain plates and shells including element subdivision. Comput Methods Appl Mech Eng 312:322–350

Assmus M, Jack S, Weiss K-A, Koehl M (2011) Measurement and simulation of vibrations of PV-modules induced by dynamic mechanical loads. Prog Photovolt Res Appl 19(6):688–694

Betsch P, Stein E (1995) An assumed strain approach avoiding artificial thickness straining for a non-linear 4-node shell element. Commun Numer Methods Eng 11(11):899–909

Bischoff M, Ramm E (1997) Shear deformable shell elements for large strains and rotations. Int J Numer Meth Eng 40(23):4427–4449

Borden MJ, Verhoosel CV, Scott MA, Hughes TJ, Landis CM (2012) A phase-field description of dynamic brittle fracture. Comput Methods Appl Mech Eng 217:77–95

Bourdin B, Francfort GA, Marigo J-J (2000) Numerical experiments in revisited brittle fracture. J Mech Phys Solids 48(4):797–826

Buerhop C, Wirsching S, Bemm A, Pickel T, Hohmann P, Nieß M, Vodermayer C, Huber A, Glück B, Mergheim J et al (2018) Evolution of cell cracks in PV-modules under field and laboratory conditions. Prog Photovolt Res Appl 26(4):261–272

Carollo V, Reinoso J, Paggi M (2017) A 3d finite strain model for intralayer and interlayer crack simulation coupling the phase field approach and cohesive zone model. Compos Struct 182:636–651

Cavuoto R, Lenarda P, Misseroni D, Paggi M, Bigoni D (2022) Failure through crack propagation in components with holes and notches: an experimental assessment of the phase field model. Int J Solids Struct 257:111798

Chaturvedi P, Hoex B, Walsh TM (2013) Broken metal fingers in silicon wafer solar cells and PV modules. Sol Energy Mater Sol Cells 108:78–81

Clayton JD, Knap J (2014) A geometrically nonlinear phase field theory of brittle fracture. Int J Fract 189(2):139–148

Clayton J, Knap J (2015) Phase field modeling of directional fracture in anisotropic polycrystals. Comput Mater Sci 98:158–169

Clayton J, Knap J (2016) Phase field modeling and simulation of coupled fracture and twinning in single crystals and polycrystals. Comput Methods Appl Mech Eng 312:447–467

Comi C, Perego U (2001) Fracture energy based Bi-dissipative damage model for concrete. Int J Solids Struct 38(36–37):6427–6454

Corrado M, Infuso A, Paggi M (2017) Simulated hail impacts on flexible photovoltaic laminates: testing and modelling. Meccanica 52:1425–1439

Dvorkin EN, Bathe K-J (1984) A continuum mechanics based four-node shell element for general non-linear analysis, Eng Comput

Forest S (2009) Micromorphic approach for gradient elasticity, viscoplasticity, and damage. J Eng Mech 135(3):117–131

Francfort GA, Marigo J-J (1998) Revisiting brittle fracture as an energy minimization problem. J Mech Phys Solids 46(8):1319–1342

Frémond M, Nedjar B (1996) Damage, gradient of damage and principle of virtual power. Int J Solids Struct 33(8):1083–1103

Gültekin O, Dal H, Holzapfel GA (2016) A phase-field approach to model fracture of arterial walls: theory and finite element analysis. Comput Methods Appl Mech Eng 312:542–566

Gültekin O, Dal H, Holzapfel GA (2018) Numerical aspects of anisotropic failure in soft biological tissues favor energy-based criteria: a rate-dependent anisotropic crack phase-field model. Comput Methods Appl Mech Eng 331:23–52

Hofacker M, Miehe C (2013) A phase field model of dynamic fracture: Robust field updates for the analysis of complex crack patterns. Int J Numer Meth Eng 93(3):276–301

Infuso A, Corrado M, Paggi M (2014) Image analysis of polycrystalline solar cells and modelling of intergranular and transgranular cracking. J Eur Ceram Soc 34(11):2713–2722

Javvaji B, Budarapu PR, Paggi M, Zhuang X, Rabczuk T (2018) Fracture properties of graphene-coated silicon for photovoltaics. Adv Theor Simul 1(12):1800097

Kajari-Schröder S, Kunze I, Eitner U, Köntges M (2011) Spatial and orientational distribution of cracks in crystalline photovoltaic modules generated by mechanical load tests. Sol Energy Mater Sol Cells 95(11):3054–3059

Käsewieter J, Haase F, Larrodé MH, Köntges M (2014) Cracks in solar cell metallization leading to module power loss under mechanical loads. Energy Procedia 55:469–477

Kiendl J, Ambati M, De Lorenzis L, Gomez H, Reali A (2016) Phase-field description of brittle fracture in plates and shells. Comput Methods Appl Mech Eng 312:374–394

Kikis G, Ambati M, De Lorenzis L, Klinkel S (2021) Phase-field model of brittle fracture in reissner-mindlin plates and shells. Comput Methods Appl Mech Eng 373:113490

Klinkel S, Wagner W (1997) A geometrical non-linear brick element based on the EAS-method. Int J Numer Meth Eng 40(24):4529–4545

Köntges M, Siebert M, Morlier A, Illing R, Bessing N, Wegert F (2016) Impact of transportation on silicon wafer-based photovoltaic modules. Prog Photovolt Res Appl 24(8):1085–1095

Köntges M, Oreski G, Jahn U, Herz M, Hacke P, Weiß K.-A. (2017) Assessment of Photovoltaic Module Failures in the Field: International Energy Agency Photovoltaic Power Systems Programme: IEA PVPS Task 13, Subtask 3: Report IEA-PVPS T13-09: 2017, International Energy Agency

Liu Z, Reinoso J, Paggi M (2022) Phase field modeling of brittle fracture in large-deformation solid shells with the efficient quasi-newton solution and global-local approach. Comput Methods Appl Mech Eng 399:115410

Liu Z, Reinoso J, Paggi M (2022) A humidity dose-CZM formulation to simulate new end-of-life recycling methods for photovoltaic laminates. Eng Fract Mech 259:108125

Liu Z, Marino M, Reinoso J, Paggi M (2023) A continuum large-deformation theory for the coupled modeling of polymer-solvent system with application to PV recycling. Int J Eng Sci 187:103842

Liu Z, Lenarda P, Reinoso J, Paggi M (2023) A multifield coupled thermo-chemo-mechanical theory for the reaction-diffusion modeling in photovoltaics. Int J Numer Meth Eng 124(12):2876–2901

Liu Z, Reinoso J, Paggi M (2022) Hygro-thermo-mechanical modeling of thin-walled photovoltaic laminates with polymeric interfaces. J Mech Phys Solids 169:105056

Matthies H, Strang G (1979) The solution of nonlinear finite element equations. Int J Numer Meth Eng 14(11):1613–1626

Mergheim J, Steinmann P (2006) A geometrically nonlinear Fe approach for the simulation of strong and weak discontinuities. Comput Methods Appl Mech Eng 195(37–40):5037–5052

Mergheim J, Kuhl E, Steinmann P (2005) A finite element method for the computational modelling of cohesive cracks. Int J Numer Meth Eng 63(2):276–289

Miehe C, Hofacker M, Welschinger F (2010) A phase field model for rate-independent crack propagation: Robust algorithmic implementation based on operator splits. Comput Methods Appl Mech Eng 199(45–48):2765–2778

Miehe C, Welschinger F, Hofacker M (2010) Thermodynamically consistent phase-field models of fracture: variational principles and multi-field Fe implementations. Int J Numer Meth Eng 83(10):1273–1311

Miehe C, Schaenzel L.-M, Ulmer H (2015) Phase field modeling of fracture in multi-physics problems. part i. balance of crack surface and failure criteria for brittle crack propagation in thermo-elastic solids, Computer Methods in Applied Mechanics and Engineering 294 449–485

Moës N, Dolbow J, Belytschko T (1999) A finite element method for crack growth without remeshing. Int J Numer Meth Eng 46(1):131–150

Msekh MA, Sargado JM, Jamshidian M, Areias PM, Rabczuk T (2015) Abaqus implementation of phase-field model for brittle fracture. Comput Mater Sci 96:472–484

Munoz M, Alonso-García MC, Vela N, Chenlo F (2011) Early degradation of silicon PV modules and guaranty conditions. Sol Energy 85(9):2264–2274

Nguyen T-T, Réthoré J, Yvonnet J, Baietto M-C (2017) Multi-phase-field modeling of anisotropic crack propagation for polycrystalline materials. Comput Mech 60:289–314

Oliver J, Huespe AE, Blanco S, Linero D (2006) Stability and robustness issues in numerical modeling of material failure with the strong discontinuity approach. Comput Methods Appl Mech Eng 195(52):7093–7114

Ortiz M, Pandolfi A (1999) Finite-deformation irreversible cohesive elements for three-dimensional crack-propagation analysis. Int J Numer Meth Eng 44(9):1267–1282

Paggi M, Wriggers P (2011) A nonlocal cohesive zone model for finite thickness interfaces-Part I: mathematical formulation and validation with molecular dynamics. Comput Mater Sci 50(5):1625–1633

Paggi M, Wriggers P (2011) A nonlocal cohesive zone model for finite thickness interfaces-Part II: Fe implementation and application to polycrystalline materials. Comput Mater Sci 50(5):1634–1643

Paggi M, Wriggers P (2012) Stiffness and strength of hierarchical polycrystalline materials with imperfect interfaces. J Mech Phys Solids 60(4):557–572

Paggi M, Kajari-Schröder S, Eitner U (2011) Thermomechanical deformations in photovoltaic laminates. J Strain Anal Eng Design 46(8):772–782

Paggi M, Lehmann E, Weber C, Carpinteri A, Wriggers P, Schaper M (2013) A numerical investigation of the interplay between cohesive cracking and plasticity in polycrystalline materials. Comput Mater Sci 77:81–92

Paggi M, Corrado M, Rodriguez MA (2013) A multi-physics and multi-scale numerical approach to microcracking and power-loss in photovoltaic modules. Compos Struct 95:630–638

Paggi M, Corrado M, Reinoso J (2018) Fracture of solar-grade anisotropic polycrystalline silicon: a combined phase field-cohesive zone model approach. Comput Methods Appl Mech Eng 330:123–148

Paggi M, Corrado M, Berardone I (2016) A global/local approach for the prediction of the electric response of cracked solar cells in photovoltaic modules under the action of mechanical loads. Eng Fract Mech 168:40–57

Papargyri L, Theristis M, Kubicek B, Krametz T, Mayr C, Papanastasiou P, Georghiou GE (2020) Modelling and experimental investigations of microcracks in crystalline silicon photovoltaics: a review. Renew Energy 145:2387–2408

Paul K, Zimmermann C, Mandadapu KK, Hughes TJ, Landis CM, Sauer RA (2020) An adaptive space-time phase field formulation for dynamic fracture of brittle shells based on LR NURBS. Comput Mech 65(4):1039–1062

Paul K, Zimmermann C, Duong TX, Sauer RA (2020) Isogeometric continuity constraints for multi-patch shells governed by fourth-order deformation and phase field models. Comput Methods Appl Mech Eng 370:113219

Peerlings R, Geers M, De Borst R, Brekelmans W (2001) A critical comparison of nonlocal and gradient-enhanced softening continua. Int J Solids Struct 38(44–45):7723–7746

Pillai U, Triantafyllou SP, Ashcroft I, Essa Y, de la Escalera FM (2020) Phase-field modelling of brittle fracture in thin shell elements based on the MITC4+ approach. Comput Mech 65(6):1413–1432

Pingel S, Zemen Y, Frank O, Geipel T, Berghold J (2009) Mechanical stability of solar cells within solar panels, Proc. of 24th EUPVSEC 3459–3464

Proserpio D, Ambati M, De Lorenzis L, Kiendl J (2020) A framework for efficient is geometric computations of phase-field brittle fracture in multipatch shell structures. Comput Methods Appl Mech Eng 372:113363

Proserpio D, Ambati M, De Lorenzis L, Kiendl J (2021) Phase-field simulation of ductile fracture in shell structures. Comput Methods Appl Mech Eng 385:114019

Reinoso J, Blázquez A (2016) Application and finite element implementation of 7-parameter shell element for geometrically nonlinear analysis of layered CFRP composites. Compos Struct 139:263–276

Reinoso J, Paggi M, Linder C (2017) Phase field modeling of brittle fracture for enhanced assumed strain shells at large deformations: formulation and finite element implementation. Comput Mech 59(6):981–1001

Rupnowski P, Sopori B (2009) Strength of silicon wafers: fracture mechanics approach. Int J Fract 155:67–74

Sander M, Dietrich S, Pander M, Ebert M, Bagdahn J (2013) Systematic investigation of cracks in encapsulated solar cells after mechanical loading. Sol Energy Mater Sol Cells 111:82–89

Simo J-C, Armero F (1992) Geometrically non-linear enhanced strain mixed methods and the method of incompatible modes. Int J Numer Meth Eng 33(7):1413–1449

Simo JC, Rifai M (1990) A class of mixed assumed strain methods and the method of incompatible modes. Int J Numer Meth Eng 29(8):1595–1638

Simo JC, Oliver J, Armero F (1993) An analysis of strong discontinuities induced by strain-softening in rate-independent inelastic solids. Comput Mech 12(5):277–296

Simone A, Duarte CA, Van der Giessen E (2006) A generalized finite element method for polycrystals with discontinuous grain boundaries. Int J Numer Meth Eng 67(8):1122–1145

Spannraft L, Steinmann P, Mergheim J (2023) A generalized anisotropic damage interface model for finite strains. J Mech Phys Solids 174:105255

Terheiden B, Ballmann T, Horbelt R, Schiele Y, Seren S, Ebser J, Hahn G, Mertens V, Koentopp MB, Scherff M et al (2015) Manufacturing 100-μm-thick silicon solar cells with efficiencies greater than 20% in a pilot production line. Phys Status Solidi (a) 212(1):13–24

Ulmer H, Hofacker M, Miehe C (2012) Phase field modeling of fracture in plates and shells. PAMM 12(1):171–172

Vu-Quoc L, Tan X (2003) Optimal solid shells for non-linear analyses of multilayer composites. I. statics. Comput Methods Appl Mech Eng 192(910):975–1016

Wang PA (2006) Industrial challenges for thin wafer manufacturing, in: 2006 IEEE 4th World Conference on Photovoltaic Energy Conference, Vol. 1, IEEE, pp. 1179–1182

Wohlgemuth JH, Cunningham DW, Placer NV, Kelly GJ, Nguyen AM, The effect of cell thickness on module reliability, in, (2008) 33rd IEEE Photovoltaic Specialists Conference. IEEE 2008:1–4

Wu J-Y, Huang Y, Nguyen VP (2020) On the BFGS monolithic algorithm for the unified phase field damage theory. Comput Methods Appl Mech Eng 360:112704

Xu X, Lai D, Wang G, Wang Y (2021) Nondestructive silicon wafer recovery by a novel method of solvothermal swelling coupled with thermal decomposition. Chem Eng J 418:129457